Tuning doping and surface functionalization of columnar oxide films for volatile organic compounds sensing: Experiments and theory

Vasile Postica,[a] Alexander Vahl,[b] Julian Strobel,[c] David Santos-Carballal, [d,ℸ] Oleg Lupan,[a,e,†] Abdelaziz Cadi-Essadek,[d] Nora H. de Leeuw,[d,f,‡] Fabian Schütt,[e] Oleksandr Polonskyi,[b] Thomas Strunskus,[b] Martina Baum,[e] Lorenz Kienle,[c,ℶ] Rainer Adelung,[e,ℷ] Franz Faupel[b,ℍ]

In this work, a new strategy based on the surface functionalization and doping of semiconducting oxides was proposed for tuning device properties. A considerable increase in the gas sensing ability of Fe-doped ZnO (ZnO:Fe) columnar films grown by chemical deposition is achieved via surface decoration with oxidized silver nanoparticles (AgO/Ag NPs) with a diameter of ~7-10 nm. AgO/Ag-decorated ZnO:Fe (Ag/ZnO:Fe) samples showed an optimal operating temperature of 300 °C with fast recovery of the signal (~ 7 s) and ultra-high sensitivity to ethanol vapor versus CH_4 and H_2 gases. The results presented demonstrate the potential for a significant increase in sensitivity to ethanol vapors by surface decoration with AgO/Ag NPs (density of ~ 0.8 × 10^9 cm^{-2}) while maintaining extremely high selectivity. Quantum mechanical simulations show that the transition metal oxide clusters modify the surface chemistry of the doped zinc oxide ZnO $(10\bar{1}0)$ surface to improve ethanol sensing. Using thermodynamic arguments, we have investigated the substitutional Fe doping of the symmetrically different Zn ions exposed at the surface. The most energetically favorable doped surface was decorated with $(AgO)_m$ nanoparticles of different sizes which were sited at different relative positions to the Fe atom. The simulated work function explains the reactivity trends of the surface models, while the scanning tunneling microscopy images are in agreement with experimental data when the $(AgO)_m$ cluster is placed over the dopant. The interface formed between the substrate and the nanoparticle is essential to enable the ethanol conversion into ethanal, suggesting that dehydrogenation plays a key role in the alcohol detection.

Introduction

Reliable detection of ethanol has become an important task for indoor and outdoor safety, as well as environmental and personal monitoring.[1-6] To that end, ethanol sensors are widely used in industry for the detection of vapors in vinification, medical processes, the food and chemical industries, and in non-invasive breathalyzers for detection of alcohol levels in motorists' breaths, e.g. modern cars with 'alcolocks' which shut down if over legal limit is detected in the driver breath.[7, 8] Semiconducting oxide micro- and nanostructures are widely used for detecting volatile organic compound (VOC) vapors such as ethanol vapors in small concentrations,[1, 6] due to their high sensitivity, low fabrication cost and low power consumption.[1, 10-13] However, the limited selectivity of pristine materials such as SnO_2 and ZnO[1, 11, 14-16] has led to the development of different modifications for improving their selectivity to specific VOCs within mixtures.[6, 9, 17-20]

In the case of ZnO, doping with transition metals or the addition of other basic metal oxides (with lower electronegativity) is known to be efficient methods that increase the ethanol response.[14, 21-27] According to Jinkawa et al.,[22] the addition of basic metal oxides can efficiently increase the ethanol response due to decomposition reaction of ethanol molecules via dehydrogenation (Eq. 1), instead of the dehydration (Eq. 2) promoted by acidic oxides: [22]

$$C_2H_5OH(g) \rightarrow CH_3CHO(g) + H_2(g) \text{ (basic oxide)} \quad (1)$$

$$C_2H_5OH(g) \rightarrow C_2H_4(g) + H_2O(g) \text{ (acidic oxide)} \quad (2)$$

Therefore, the decomposition of ethanol molecules into $CH_3CHO + H_2$ after oxidation with adsorbed oxygen species on the surface of the metal oxide induces a larger change in carrier concentration, i.e. higher gas response.[21, 22]

In our previous work, Fe-doping of ZnO nanostructured films resulted in a considerable increase in ethanol sensing properties (by a factor of two), as well as fast response and recovery times (1 – 2 s).[14] In the current work, the AgO/Ag decorated ZnO:Fe nanostructured films led to a change in resistivity by a factor of 63 after introduction of 20 ppm of ethanol vapors in the test chamber. However, modern gas sensing systems for the detection of ethanol, especially in human breath, require highly sensitive ethanol sensors (ppm level).[30] Thus, in this work, in order to improve the sensitivity to ethanol vapors of earlier elaborated ZnO:Fe nanostructured films, we have applied decoration with Ag NPs with a diameter of < 10 nm, which did not result in any loss in selectivity. The choice of Ag NPs was motivated by their excellent catalytic properties.[1, 10, 17, 28, 31] Furthermore, we also present a computational description by means of density functional theory (DFT) calculations of the Fe-doped zinc oxide ZnO $(10\bar{1}0)$ surface decorated with AgO nanoparticles as a highly selective sensor for ethanol vapours. We propose models that account for the modified ZnO $(10\bar{1}0)$ surface, which are fully characterized using scanning tunneling microscopy images and work function values. We have also examined the adsorption energies of ethanol, ethanal, methane and molecular hydrogen and the electron charge density redistribution upon

[a.] *Department of Microelectronics and Biomedical Engineering, Technical University of Moldova, 168 Stefan cel Mare Av., MD-2004 Chisinau, Republic of Moldova.*
[b.] *Chair for Multicomponent Materials, Institute for Materials Science, Kiel University, Kaiserstr. 2, D-24143, Kiel, Germany.*
[c.] *Synthesis and Real Structure, Institute for Materials Science, Kiel University, Kaiser str. 2, D-24143, Kiel, Germany.*
[d.] *School of Chemistry, Cardiff University, Main Building, Park Place, Cardiff CF10 3AT, United Kingdom.*
[e.] *Functional Nanomaterials, Institute for Materials Science, Faculty of Engineering, Kiel University, Kaiserstr. 2, D-24143, Kiel, Germany*
[f.] *Department of Earth Sciences, Utrecht University, Princetonplein 8A, 3584 CB Utrecht, The Netherlands.*
† Corresponding author: e-mail ollu@tf.uni-kiel.de
ℸ e-mail SantosCarballalD@Cardiff.ac.uk
‡ e-mail deLeeuwN@cardiff.ac.uk, n.h.deleeuw@uu.nl
ℶ e-mail lk@tf.uni-kiel.de
ℷ e-mail ra@tf.uni-kiel.de
ℍ e-mail ff@tf.uni-kiel.de

interaction with the modified ZnO $(10\bar{1}0)$ surface, to rationalize its selectivity towards the alcohol.

Experimental

ZnO:Fe columnar films were deposited on glass substrates according to the procedure reported in previous works,[14, 34, 35] where the morphological, structural, micro-Raman, chemical and electrical properties were investigated in detail. In this study, we used the samples with 0.24 at% Fe content and thickness of ~ 1.5 µm to functionalize their surface with Ag nanoclusters. In addition to decorating ZnO:Fe with Ag NPs, the nanoparticles were also deposited onto silicon wafer pieces (1 × 1 cm², SIMat) for XPS measurements and on carbon film copper TEM grids (Plano, S160-4) for TEM investigations.

For the synthesis of Ag nanoparticles an in-house Haberland type Gas Aggregation Source (GAS)[36] attached to a custom-made vacuum deposition chamber primarily built from commercially available components was used.[37-39] This physical vapor deposition method generates nanoparticles from individual metal atoms, which are brought into the gas phase by sputtering. Firstly, metallic nuclei are formed in a three-body collision process, where the third collision partner is a gas atom that takes away the excess energy to prevent the nucleus from disintegrating. The stable nuclei undergo subsequent collisions with further metal atoms or other nuclei, favoring growth of coalescence, respectively. The pressure difference between the GAS and the high vacuum chamber is responsible for driving the nanoparticle beam towards the substrate. A full coverage of the basic principles for the growth mechanism of nanoparticles using GAS can be found elsewhere.[40]

An Ag target (Kurt J. Lesker, 99.99 %, 50 mm diameter) was attached to a DC planar magnetron source (Thin Film Consulting, ION'X-2UHV) inside the GAS. The samples are mounted at a distance of 90 mm from the exit orifice (diameter 2 mm) of the GAS, the sample surface was perpendicular to the nanoparticle beam.

The deposition chamber was evacuated to at least 10^{-4} Pa using a turbo molecular pump (Pfeiffer Vacuum, TMU 262) and a dry scroll pump (Agilent Technologies, SH-110). For sputtering, a flow (48 SCCM) of Ar (purity 99.999%) was supplied at the gas inlet of the GAS (gas regulating valve: Pfeiffer, EVR116 with attached hot ion cathode IMR 285). During each deposition the pressure inside the GAS was typically 136 Pa. The nanoparticles were generated from silver atoms sputtered by DC unipolar magnetron sputtering with a DC power of 40 W (Advanced Energy, MDX 500). Prior to every deposition process, the target was cleaned and nanoparticle growth was conditioned for a sufficient time (at least 30 s) to reach stable deposition conditions. More details on the deposition of Ag nanoparticles from a GAS are reported in Ref. [43]. After deposition samples were subjected to thermal annealing in air at 350 °C for 1 h. More details of the influence of deposition on the mechanism of Ag NPs growth were presented in previous works.[37-39]

The morphological, structural, optical, chemical and gas sensing properties of oxide columnar films, including ZnO:Fe were investigated as described in previous works.[14, 33, 44] Micro-Raman spectra were recorded with a Raman WITec Alpha300 RA spectrometer (532 nm line from a Nd-YAG laser was used for excitation). Transmission electron microscopy (TEM) analysis was conducted in a FEI Tecnai F30 STwin microscope (300 kV, field emission gun (FEG) cathode, spherical aberration coefficient Cs = 1.2 mm). Particle size distribution and density were determined in TEM bright field mode and high-angle annular dark field (HAADF) scanning TEM (STEM) mode.

The chemical composition of the deposited nanoparticles was investigated by X-ray photoelectron spectroscopy (XPS, Omicron Nano-Technology GmbH), operating with an Al-anode at a power of 240 W. The recorded spectra were charge referenced by using aliphatic carbon C-1s at 285.0 eV using the software CasaXPS (version 2.3.16). The sensor structures for investigation of gas sensing properties were fabricated using the method described in previous work.[14] The gas sensing measurements were performed at different operating temperatures, as was described in previous works.[44, 45] Ambient air with a relative humidity of 30 – 40% was used as the carrier gas forthe analyte vapors.

The details of the computational methods used, including calculation details, surface models, calculation of surface energy and adsorption energy, simulation of the scanning tunneling (STM) images and work function are presented in **Supporting Information**.

Results and discussion

Morphological and micro-Raman properties

Figure 1 shows the SEM images of AgO/Ag-decorated nanostructured ZnO:Fe films. The morphological properties of pristine ZnO:Fe samples, with the same Fe content of 0.24 at%, were provided in a previous publication.[14] After decoration with AgO/Ag NPs the morphology of the nanostructured ZnO:Fe films was not modified. The diameter of AgO/Ag-decorated ZnO:Fe grains is in the range of 100 to 400 nm. The grains are densely packed on the glass substrate (see **Figure 1a,b**). As can be observed from **Figure 1c**, AgO/Ag NPs are well dispersed on the surface of ZnO:Fe grains and their density reaches a value of ~ 0.8×10^9 cm^{-2}. The illustration of the gas sensor fabrication based on ZnO:Fe and Ag/ZnO:Fe nanostructured films is presented in **Figure 1d**, while the overall sensor structure is presented in **Figure 1e**. More details on the synthesis and Ag NP deposition can be found in the Experimental part.

A typical room-temperature Raman spectrum of the as-prepared AgO/Ag-functionalized ZnO:Fe nanostructured films is presented in **Figure 2a**, with the spectrum assignable to typical wurtzite ZnO. The peaks at 100, 204, 330, 408, 547 and 583 cm^{-1} can be assigned to E_2(low), $2E_2$(low), E_2(high) - E_2(low), E_1(TO), E_2(high), A_1(LO), and E_1(LO) phonon modes.[46] Additional peaks were observed at 217, 301 and 379 cm^{-1}, which can be assigned to AgO phonon modes.[47] From group analysis, the optical modes at the Γ point belong to the following irreducible representation:[47]

$$\Gamma = 8A_u(IR) + 7B_u(IR) + 3A_g(R) + 3B_g(R) \quad (3)$$

where *IR* and *R* indicate the infrared and Raman active modes, respectively. The peak at 429 cm^{-1}, which is attributed to AgO and usually has a higher intensity, can be superimposed on E_1(TO) and E_2(high) phonon modes of ZnO[47, 48] is therefore difficult to detect here.

Chemical properties

An AgO/Ag-functionalized ZnO:Fe sample and a reference sample of AgO/Ag NPs (on a silicon wafer piece) were measured by XPS for comparison. In **Figure 2b** the overview spectra of the nanocomposite (black line) and the AgO/Ag NPs reference (red line) are shown. The overview spectra were analyzed for elemental composition and the respective characteristic peaks were marked in the spectra. For the AgO/Ag-functionalized ZnO:Fe nanostructured films, the elements Zn, O, C, Ag and Au were detected, where the occurrence of Au is attributed to the top contacts on the sample surface. The presence of C originates from atmospheric surface contamination, e.g. hydrocarbons.[48, 49] The ZnO:Fe base layer has been extensively studied in our earlier work, showing the presence of Fe in the XPS spectrum of the pure ZnO:Fe layer[14] as shown in the Supporting Information (see **Figure S1**). However, in the case of the AgO/Ag-functionalized ZnO:Fe nanostructured films we do not observe any characteristic peaks for Fe, which may be attributed to the coverage of the ZnO:Fe base layer by AgO/Ag NPs and consequently a weakening of the Fe signal below the limit of XPS detection. Moreover, in the present work no surface pre-cleaning was performed prior to the XPS analysis, in contrast to the previous work.[14, 44, 45, 50] The XPS investigation of a highly doped ZnO:Fe thin film, proving the successful incorporation of iron as a doping element, can be found in the supporting material (see **Figure S1**).

In the Ag NPs reference (see **Figure 2b**, red line), the elements Ag, O, C and Si were detected, where again the occurrence of C is due to surface contamination. The native oxide layer of the Si wafer substrate resulted in the presence of Si and O peaks. The comparison of Ag-3d peaks (**Figure 2c**) in both samples shows a shift of the Ag peak to lower binding energies in case of the AgO/Ag-functionalized ZnO:Fe nanostructured films (by roughly 0.3 eV). Typically, a binding energy of around 368.2 eV is attributed to metallic Ag, whereas its oxides are shifted to lower binding energies of about 367.9 eV (Ag2O) and 367.6 eV (AgO) respectively.[51] The observed shift in the nanocomposite may be attributed to (surface) oxidation of the nanoparticles. For reference, the C-1s lines at 285.0 eV are compared in **Figure 2d**.

Structural properties

The XRD patterns of ZnO:Fe nanostructured films were discussed in our previous work.[14] The formation of the secondary phases of Fe, its oxides (FeO, Fe_2O_3 or Fe_3O_4) or impurities were not observed, indicating that only the hexagonal crystalline phase of ZnO is present.[14] Ag NPs were analysed by TEM not only after deposition onto ZnO:Fe (see **Figure 3** top row) but also onto empty carbon films (see **Figure 3** bottom row) to serve as a reference to determine size distribution. The selected area electron diffraction (SAED) pattern of AgO/Ag NPs on ZnO:Fe, **Figure 3a,** shows reflections for the AgO planes (-111), (-202) and (020) at experimentally determined lattice spacings of 2.76 Å, 2.21 Å and 1.72 Å respectively, which are characteristic for AgO and do not match any of the other phases, thereby emphasizing the slight oxidation of the NPs. **Figure 3c** shows the uniform distribution of AgO/Ag particles on ZnO; it should be noted that they are only visible near the fringes of the ZnO microcrystals due to considerable thickness of the latter. For the same reason no high resolution and energy-loss spectroscopy could be conducted. For comparison purposes, Ag particles have also been deposited onto blank carbon film TEM grids. The bottom row of **Figure 3** shows that only reflections for pure Ag are found (Figure **3d**) which exhibit a bimodal size distribution with maxima at around 2.0 ±0.7 nm and 7.6 ±2.8 nm. All examined particles are completely crystalline, and an example showing the characteristic fivefold twin is displayed in **Figure 3f**.[52] It is noteworthy, that the particles deposited onto carbon films show no oxidation but instead suffer a pronounced sulfidation after storing them for intermediate time periods, as is expected for Ag nanostructures.[53] The oxidation of Ag NPs deposited onto ZnO:Fe columnar crystals is thus attributed to a combination of ballistic effects and the increased temperature of Ag during the deposition process, thereby locally reducing the ZnO and simultaneously oxidizing the silver. Note, that the reduction of ZnO is not detectable directly from the Zn-2p XPS lines because it causes only a negligible shift of the binding energy.[54] Although AgO decomposes in ambient atmosphere above 150 °C to Ag_2O,[55] it has been shown that an AgO/Ag_2O mixture forms during annealing at 400 °C in a 10% O_2 atmosphere.[56] We therefore deem this scenario more likely than oxidation in ambient atmosphere, as the latter has not been observed previously.

Gas sensing investigations

Figure 4a shows the gas response to 20 ppm of ethanol, 1000 ppm of hydrogen (H_2) and 1000 ppm methane (CH_4) gases versus operating temperature for the AgO/Ag-decorated ZnO:Fe columnar film. The operating temperature was set in the range of 150 – 350 °C. The gas response (*S*) was defined as the ratio of the current under exposure to gas (I_{gas}) and in air (I_{air}). Error bars represent the standard deviation for the response of each sensor structure after several measurements. At room temperature and near room temperature no response to ethanol vapors and other gases was observed. The content of Fe in the studied samples is 0.24 at%, as in the previous study.[14] For ethanol vapors the optimal operating temperature is 300 °C with a response of S ≈ 63. The optimal operating temperature is comparable with those of pristine ZnO:Fe columnar films (see **Figure 4b**), but as can be observed from **Figure 4b**, the response of the Ag-decorated sample to 20 ppm of ethanol is higher compared to the pristine ZnO:Fe film. For example, at 300 °C the response of Ag/ZnO:Fe is *S* ≈ 63 compared to *S* ≈ 15 of the non-decorated (pristine) ZnO:Fe. This corresponds to enhancement by a factor of 4 after functionalization of ZnO:Fe surface with

AgO/Ag nanoclusters. The dynamic response of nanostructured Ag/ZnO:Fe films to different concentrations of ethanol vapors is presented in **Figure 4c**, showing a reversible response with a stable electrical baseline. After introduction and extraction of 500 ppm of ethanol, we also introduced twice a concentration of 150 ppm of ethanol to check the repeatability of the response, showing a deviation lower than 5%. The gas response versus concentration of ethanol vapors in a *log.* versus *log.* plot is presented in **Figure 4d**. For concentrations of 20, 50, 100, 150, 250 and 500 ppm the response (*S*) is roughly 63, 86, 104, 120, 147 and 175, respectively. As can be observed, the response (*S*) follows a power law relationship with ethanol concentration ($S \propto p_{EtOH}^{\beta}$), where β ≈ 0.45 is the slope of the *log.* versus *log.* plot. Using the method described by Dua *et al.*, i.e. using the signal/noise ratio (SNR),[5] we calculated a theoretical detection limit of ~ 0.35 ppm. In the case of the response to 100 ppm of H_2 the SNR is ~ 312, while for 20 ppm is ~ 62, which is much higher than the minimum value of 3 defined by IUPAC.[57] The gas response to 20 ppm of ethanol vapors was also measured at higher concentration of water vapors (~ 80%), showing a decrease of the response to ~ 35 (decrease by factor of 1.8, not shown). This effect can be explained based on poisoning by hydroxyl-groups, which has already been discussed in previous works.[12, 50, 58]

The response and recovery times were defined as the time necessary to obtain or recover 90% of the full response.[59] The estimated values for response and recovery times are presented in **Figure 4e**. In both cases, the values are improved by raising the operating temperature from 150 to 350 °C. The response time decreases from ~ 141 s at 150 °C to ~ 22 s and ~ 13 s at 300 and 350 °C, respectively, while the recovery times decrease from ~ 61 s at 150 °C to ~ 7.2 s and ~ 3 s at 300 and 350 °C, respectively.

From **Figure 4a** it can be observed that nanostructured AgO/Ag-functionalized ZnO:Fe films possess high selectivity to ethanol vapors, i.e. a higher response to 20 ppm of ethanol vapor compared to 1000 ppm of H_2 and CH_4 gasses. The evaluation of sensor response selectivity was performed by cross-interference of H_2 and CH_4 gases with ethanol vapors. The H_2 and CH_4 (1000 ppm) cross sensitivity to 20 ppm of ethanol vapors was also evaluated. **Figure 4f** shows the dynamic gas response to 1000 ppm of H_2 and CH_4 gases in air + 20 ppm of ethanol vapors atmosphere. No considerable deviations in response after introduction of 1000 ppm of H_2 and CH_4 gases were observed, demonstrating excellent selectivity to ethanol vapors without interference from other gases. **Figure S2** also shows the gas response to 1000 ppm of H_2 and CH_4 gases and 20 ppm of ethanol vapors at 300 °C, introduced in the test chamber one at a time, also showing excellent selectivity to ethanol vapors. **Figure S6** shows the long-term stability of Ag/ZnO:Fe nanostructured films at 300 ◦C for 20 ppm of ethanol vapors, demonstrating good stability of the material.

Table 1 summarizes several recent results on high performance ethanol sensors based on metal oxide micro- and nanostructures, as well as other Ag-decorated ZnO nanostructures in order to compare with our results. Our experiments show that the AgO/Ag NPs decorated ZnO:Fe columnar films exhibit properties that are better or on a par with most reports. Taking into consideration the excellent selectivity of our Ag/ZnO:Fe nanostructured films and rapid recovery, our samples are excellent candidates for high performance ethanol sensors and in addition allow significant customization in terms of for example the transition metal dopant, its doping concentration, nano-particle quantity, composition and size.

The sensing mechanism which was reported in our previous work explains the excellent reactivity of ZnO:Fe nanostructured films towards ethanol compared to the undoped films based on the catalytic effect of the Fe dopant, facilitating the speed of the response and recovery reactions during detection of ethanol.[14] At operating temperatures higher than 200 °C, mainly atomic oxygen species are adsorbed on the surface of ZnO:Fe nanocrystallites which are ionized when they capture free electrons.[60] This will form an electron depletion region at the surface of the nanocrystallites with the highest resistivity and the largest number of potential barriers between nanocrystallites.[14, 20, 50, 60, 61] After introduction of ethanol vapors in the test chamber, ethanol molecules will oxidize via the following reaction:[14, 25, 26, 62]

$$CH_3CH_2OH_{(ads)} + 6O^-_{(ads)} \rightarrow 2CO_{2(g)} + 3H_2O_{(l)} + 6e^- \qquad (4)$$

Table 1. Ethanol vapor gas sensors based on *n*-type semiconducting oxides

Sensing material	EtOH conc. (ppm)	Gas response (R_{air}/R_{gas}) or (R_{gas}/R_{air})	Operating temperature (°C)	Response time (s)	Recovery time (s)
Ag-doped ZnO-SnO_2 hollow nanofibers [1]	1	7.6	200	5	5
Ag/ZnO nanorods [9]	100	36.52	360	50	28
ZnO-Ag hybrids [17]	100	101.8	370	~ 15	~ 20
Ag-ZnO films [28]	2000	~ 2	225	5	-
Ag-doped ZnO films [29]	100	~ 15	260	-	-
Ag-(TiO_2/SnO_2) [18]	50	53	275	3.5	7
In_2O_3-ZnO nanocomposites [15]	300	900	250	25	1100
Ag/TiO_2 nanoparticles [10]	5	4.35	RT	52	63
In_2O_3 hollow nanorods [32, 33]	100	38.6	200	3	4
Au/ZnO NWs [6]	100	33.6	380	3	1
ZnO:Fe films [14]	100	61	250	1.1	1.45
CuO hollow nanostructures [41]	3500	~ 7	200	-	-
(CuO-Cu_2O)/ZnO:Al heterojunctions [42]	100	~ 1.6	350	-	-
CuO/Cu_2O nano-crystalline films [45]	100	~ 9.5	275	4.1	10.5
Ag/ZnO:Fe films (This work)	20	63	300	22	7.2

This will result in a narrowing of the electron depletion region and a decrease in the potential barrier height, i.e. change in current density.[14, 60] Therefore, the gas response (S) depends on the modulation of the electron depletion region and change in potential barrier height ($e\Delta V_s$) between columns and nanocrystallites:[14, 60]

$$S \approx \exp\left(-\frac{e\Delta V_S}{2kT}\right) \quad (5)$$

where k is the Boltzmann constant and T is the absolute temperature.

In the present work, the further improvement in the ethanol vapor sensing and fast recovery of our samples can be explained on the basis of the excellent catalytic properties of the Ag nanoclusters. Ag functionalization accelerates the oxidation reactions of the ethanol molecules,[17, 31] as well as the transfer of electrons or negatively charged adsorbed oxygen, O^-, to the surface of ZnO:Fe during the recovery reaction.[63]

Theoretical calculations

ZnO has the wurtzite structure characterized by the space group P63*mc* (No. 186).[64] **Figure 5a** displays the conventional hexagonal unit cell with two formula units (f.u.). Each atomic sublattice forms a hexagonal close-packed (*hcp*) arrangement along the [0001] direction. Each ion type is tetrahedrally coordinated to the atoms of opposite charge, implying that half of the tetrahedral sites are empty. The Zn ions are distributed in the Wyckoff *2b* tetrahedral positions with coordinates (1/3, 2/3, 0), while the O atoms also occupy the *2b* crystallographic sites, lying above the cations at (1/3, 2/3, *u*). The *u* value represents the Zn–O interatomic distance in fractional coordinates in the ZnO bulk, which holds the relationship $u = \frac{a \cdot \sqrt{(3/8)}}{c}$ with the *a* and *c* lattice parameters for the perfectly hexagonal material.

Table S1 shows the calculated relaxed lattice edges for the hexagonal unit cell of ZnO bulk, which are slightly underestimated by between 0.05 to 0.07 Å with respect to experiments.[64] The internal coordinates were fully optimized, with both types of ions remaining in their ideal Wyckoff *2b* crystallographic positions. We found a negligible difference between the independent oxygen *u* parameter and the nearest neighbours distance, indicating an undistorted tetrahedral coordination for the Zn and O atoms. Although the shape of the conventional unit cell was also allowed to relax, it remained perfectly hexagonal, with an equilibrium volume of $\bar{V} = 26.294\,\text{Å}^3$ f.u.$^{-1}$. The calculated Bader charges[65-68] are 1.187 e$^-$ for Zn and −1.187 e$^-$ for O, which represent the number of electrons transferred between the neutral atoms upon the formation of ZnO bulk. These charges are ~40% below the formal atomic oxidation state of 2+ and 2− for the Zn and O atoms, respectively, which is a known effect in Bader charges.[69, 70] The calculated electronic band gap of 1.80 eV for ZnO bulk is underestimated at 53% of the experimental value,[71] which is a known artifact of DFT simulations where the correlation of excited electrons is ignored.[72]

We provide further computational insight by firstly modeling the pristine terminations A and B of the low Miller index $(10\bar{1}0)$ surface of ZnO, shown in **Figure 5b** and **5c**, respectively. From our simulations of the surface energies, which are summarized in **Table S2**, we have inferred that termination B is the most stable surface, both before and after relaxation, which led to the largest percentage relaxation reported in this study.

The stacking sequence of ZnO in the $[10\bar{1}0]$ direction and the vertical atomic displacements towards the vacuum after geometry optimizations are shown in **Figure 5b** and **5c**. The top surface layer of terminations A and B have a bulk-like structure, comprising alternating rows of 2-coordinated O and 2-fold Zn ions in the $[10\bar{1}0]$ direction. Structurally, terminations A and B only differ by the interlayer spacings between the exposed plane and the one beneath, which are 1.848 and 0.924 Å, respectively. Following relaxation of termination A, the top Zn atoms moved 0.27 Å towards the bulk and 0.36 Å in the $[0001]$ direction, causing the O ions of the same layer to migrate 0.12 Å outward and 0.09 Å in the $[0001]$ direction, becoming closer to each other by 0.22 Å. In contrast, the Zn atoms of the subsurface layer shifted towards the surface, by just ~54% of the displacement of the cations in the top layer. The Zn ions in the remaining layers relaxed in turn in the opposite direction with respect to the surface, while the O atoms of all the subsurface layers always moved towards the vacuum during optimization. However, the atomic displacement was less than 0.05 Å and was increasingly attenuated for every layer towards the bulk. We found for termination B that the undercoordinated Zn atoms are the only ones that experience any noticeable displacements, calculated at 0.30 Å inward and ~56% of this value in the $[0001]$ direction.

Despite the lack of magnetism in any of the ZnO $(10\bar{1}0)$ surfaces, we found different charge rearrangements in terminations A and B. The 2-fold O atoms gain 0.20 e$^-$ from the 2-coordinated Zn with respect to the charges in the bulk, whereas the electron transfer is negligible for termination B. Moreover, our simulations indicate that the work function of termination A is 0.40 eV lower than for termination B, which stands at 5.80 eV. This suggests that the oxygen-rich electrons from termination A are easier to remove and are more available than in termination B.

Based on these results we have analyzed the process of substitutional doping of the ZnO lattice by Fe ions and its impact on the thermodynamic stability of the surface, the atomic charges and spin moments, as well as the work function. From experiment, we know that the Fe content of the samples is ~0.24 at%, which corresponds to 0.12 ions in a 48 f.u. supercell. Thus, given the size of our surface slab and to avoid unrealistic decimal numbers of dopant atoms, we decided to model 1 Fe substitution (2.08 at%), which is the closest integer number. We have doped both terminations, A

and B, to study any changes in relative stability due to the substitution. Only the doping of the exposed 2- and 4-fold Zn sites were considered in the surface and subsurface according to,

$$Zn_{48}O_{48}\left(10\bar{1}0\right)+Fe(s)=Zn_{47}FeO_{48}\left(10\bar{1}0\right)+Zn(s) \quad (6)$$

The surface free energies of the Fe-doped systems, which are listed in **Table S2**, show that substitution of any of the exposed Zn atoms is an exothermic process. The dopings of termination A sites release by far the largest energies, yet this is still not enough for A to become the most stable termination. For the most favorable doping, the substitution of the 2-coordinated Zn brings ~3 meV·Å^{-1} of stabilization to termination B, which remains the major surface. Small shifts in the positions of the surface atoms, of the order of less than 0.05 Å, due to the Fe insertion argue in favor of the nil stabilization of termination B. We found that 2-fold Zn substitution is more stabilizing than doping the 4-fold position, regardless of whether they are in termination A or B, in agreement with their more prominent exposure.

Zn substitution has a clear effect on the electronic and magnetic properties of the surfaces. The introduced Fe atoms lose more than 1 e$^-$ with regards to the neutral atom after replacing the surface Zn ions. The 2-fold Fe becomes more positive after substitution, especially in termination B, than the 4-coordinated Fe. The doping of termination A also induces a concomitant oxidation of 0.10 e$^-$ of the remaining topmost Zn atoms. The electronic charge is largely transferred to the topmost O atoms, where each gains an average of 0.15 e–. Based on the average magnetic moment of 4 μB·atom^{-1} for the Fe atoms, we can assign them an oxidation number of 2+. The electronic distribution $e_{\uparrow}^{2}e_{\downarrow}^{1}t_{2\uparrow}^{3}$ is in reasonable agreement with Fe^{2+} ions in a pseudo-tetrahedral crystal field of oxygen ligands, particularly in the 4-coordinated sites and in termination B.

Our simulations suggest that following doping, the work function is halved with respect to the pristine surfaces, see **Table S2**, lending support to the increased reactivity of this system.[14] Moreover, the work function value can be controlled by the coordination of the site occupied by the dopant atom. For example, doping of the 2-coordinated site leads to a work function of ~2.36 eV, while substitution of the 4-coordinated Zn reduces this magnitude to 2.51 eV. We do not consider the doped slabs of termination A or the 4-fold site of termination B for further analysis because of their higher surfaces energies, which make them very unlikely to appear in the ZnO crystal morphology.

Additional modifications by adsorbing $(AgO)_m$ clusters, where 0 ≤ m ≤ 6, were also carried out to evaluate the further functionalization of the Fe-doped ZnO surface towards selective detection of ethanol vapours. The $(AgO)_m$ particles were incorporated in three different relative positions to the Fe dopant, i.e. i) above, ii) close by, and iii) far away. The initial $(AgO)_m$ geometries were chosen based on small particles derived from monoclinic AgO.[73] Our simulations suggest that the addition of AgO in only three scenarios reduces the value of the surface free energy with respect to the doped surface, i.e. when 1 f.u. of AgO is placed above and close to the Fe or when the dopant is underneath the $(AgO)_3$ cluster, see **Table S3**. In general, the calculated surface free energy of the fully modified surface increases slowly with *m*, mainly when the cluster is close by or far away from the dopant. The calculated clustering energies for the AgO nanoparticles are also in agreement with the trend in surface free energies. Our DFT modeling predicts that the adsorption of small AgO clusters of up to *m* = 3 f.u. is thermodynamically unfavorable as the clustering energy is negative in some cases. However, the cohesive forces become more important for clusters of *m* ≥ 4 f.u. when the growth of the nanoparticles is thermodynamically favorable.

We found that the work function increases gradually with *m* upon adsorption of the $(AgO)_m$ particles, and reaches a maximum value of 3.14 eV at *m* = 6. Our calculations show that the atomic magnetic moments and charges of the Fe-doped ZnO films substrate are not noticeably affected following the introduction of the AgO clusters. As expected, Ag is oxidized by losing 0.65 e$^-$, while the O atoms from the nanoparticle are reduced by the same amount.

To simplify the analysis of the fully modified surfaces, we focus the rest of the characterization on the case where the $(AgO)_5$ nanoparticle is adsorbed above the Fe dopant. This choice of cluster size will also allow us to discuss the interaction with small molecules by using the largest possible isolated nanoparticles without lateral inter-particle interactions.

The mimicked STM topographic image displays the regularly repeated $(AgO)_5$ clusters sitting on the Fe-doped ZnO surface, see **Figure 5d**, which resemble the well dispersed scanning transmission electron microscopy high-angle annular dark field (STEM-HAADF) image from experiments. The overall agreement between these simulated and experimental techniques provides strong support for the reliability of our functionalized surface model.

We next investigated the interaction of the molecules present in the test chamber, i.e., CH_4, H_2 and CH_3CH_2OH as well as its dehydrogenation product CH3CHO, with the fully modified ZnO $\left(10\bar{1}0\right)$ surface. In a series of calculations, we studied the single molecule adsorption by placing the adsorbates in different orientations at 1.5 Å from the surface. The molecules were introduced at three relative positions to the $(AgO)_5$ cluster, i.e. interacting solely with either the particle or the ZnO $\left(10\bar{1}0\right)$ surface and close to the interface formed between them. **Table S4** summarises the calculated adsorption energies, indicating that their increasing strength of binding is $H_2 \approx CH_4 \ll CH_3CHO < CH_3CH_2OH$, regardless of the relative position to the $(AgO)_5$ cluster. This order suggests a larger preference for the interaction with the C_2 compounds than with the H_2 or CH_4 molecules, in agreement with the gas response experiments. We observe that the non-polar molecules release the largest adsorption energies for the almost degenerate interactions with either the ZnO $\left(10\bar{1}0\right)$ surface or the interface between surface and cluster.

We found that H_2 adsorbs molecularly for any of the interaction configurations, in contrast to reports in previous studies of the pristine and doped Zn (0001) surfaces.[11, 26, 62] For the least likely adsorption mode, the H_2 molecule prefers to be

sited at 2.27 Å atop one of the most exposed Ag atoms. Moreover, H_2 binds at the interface interacting with a Zn cation at 2.10 Å and simultaneously with a neighboring O atom from the AgO cluster at 1.90 Å. The distance between H_2 and Zn was 0.07 Å larger than between the adsorbate and a surface oxygen, when the molecule is placed away from the $(AgO)_5$ cluster. Our simulations indicate that the H_2 intramolecular distance experiences a minor elongation with respect to the isolated molecule (between 0.76 and 0.79 Å) upon adsorption on the cluster, at the interface or on the surface. The estimated charge rearrangement after H_2 adsorption is negligible.

The CH_4 molecule also physisorbs in the three interaction configurations considered in this study, in line with earlier works.[26, 62] The CH_4 molecule is not able to stay closer than 3.20 Å to any atom from the $(AgO)_5$ cluster in the weakest adsorption configuration. However, one of the H atoms has a small affinity to interact at 2.46 Å with one of the O ions from the cluster or the surface when the CH_4 molecule is placed in the vicinity of the interface or away from the nanoparticle, respectively. The C−H bond distances and H−C−H bond angles are 1.10 Å and 109°, respectively, which are very similar to the ones calculated for the isolated molecule. The Bader analysis shows that CH4 remains electrically neutral following adsorption, which is expected for physisorbed molecules.

The adsorption energies reveal that the least favorable adsorption sites for CH_3CHO are the cluster and the interface, which show similar affinity. The aldehyde binds to the $(AgO)_5$ nanoparticle through the formation of HCHO−OSURF and OCHO−Ag bonds of lengths 1.98 and 2.20 Å, respectively, where CHO represents atoms from the polar carbonyl group and SURF represents surface atoms. Our calculations predict that CH3CHO will be slightly more detached from the substrate in the degenerate adsorption mode at the interface than above the particle. In this adsorption mode, the aldehyde molecule is able to bridge two neighbouring $(AgO)_5$ clusters given their proximity, forming O_{CHO}−Ag and H_{CH3}−O_{SURF} bonds of lengths 2.38 and 2.20 Å, respectively, where CH_3 represents the methyl group. In the most stable adsorption site, away from the $(AgO)_5$ nanoparticle, the carbonyl oxygen is binding a Zn ion at 2.13 Å, while one of the methyl hydrogen connects to a surface oxygen atom at 1.96 Å. Following adsorption, we found that the intramolecular C−O distance is stretched by 0.02 Å, while the carbonyl H−C−O bond angle is changed from 120° to 118° with respect to the isolated aldehyde molecule. Our DFT simulations estimate that the molecule will donate 0.16 and 0.07 e^- charge when adsorbed on the cluster and at the interface, respectively.

CH_3CH_2OH interactions with the cluster/surface interface in the least and most favorable adsorption modes are shown in **Figure 5e** and **5f**, respectively. These configurations can be viewed as the initial and final states of the spontaneous alcohol dehydrogenation reaction, with an exothermic enthalpy of −3.33 eV. The simulation of the structure of the initial and least preferred configuration indicates that the alcohol adsorbs molecularly. The hydroxyl H forms a hydrogen bond to one surface O at 1.56 Å, while the hydroxyl O weakly coordinates to one Ag atom at 2.42 Å. During the dehydrogenation process, we found that the O−H bond breaks and the CH_3CH_2OH molecule rotates to allow the scission of the C_α−H bond. This leads to the formation of two hydroxy groups, one formed with a surface oxygen and the other with a cluster oxygen, as well as the CH_3CHO molecule fragment adsorbed to the surface. We also found another adsorption configuration above the $(AgO)_5$ cluster, where the CH_3CH_2OH interacts dissociatively by donating only the hydroxy H to one cluster oxygen. We have elucidated for the molecular adsorption configuration that the ethanol O−H distance is slightly elongated by 0.05 Å as the H forms one hydrogen bond with a surface oxygen. However, for the interaction mode where only one H is donated to the cluster, the C−O distance shortens by 0.03 Å. Elimination of the second H further reduces the C=O distance to 1.24 Å, which is now typical of a double bond. The adsorbate donates to the surface 0.28 e^- charge for the molecular adsorption and the mode where the molecule loses one H. However, the largest adsorbate-to-substrate charge transfer of this study is calculated at 1.29 e^- for the case where the CH_3CH_2OH molecule dehydrogenates to form CH_3CHO, in agreement with the enhanced sensing properties of the Fe-doped ZnO $(10\bar{1}0)$ surface decorated with the $(AgO)_m$ clusters.

Conclusions

In summary, the ZnO:Fe columnar films were successfully functionalized/decorated with AgO/Ag NPs by a new strategy. Systematical investigations demonstrate that Ag NPs have bimodally distributed diameters of around 7 and 10 nm respectively and are slightly oxidized on the surface. The gas sensing results underline that Ag-decoration is highly efficient to effect considerable increase in sensitivity to ethanol vapors (gas response to 20 ppm increased from ~ 15 to ~ 63), without change in selectivity. Even after introduction of H_2 and CH_4 gases with much higher concentration (1000 ppm) in the presence of 20 ppm of ethanol vapors in the test chamber no changes in current are produced, which demonstrates the high selectivity of nanocluster-fuzed AgO/Ag/ZnO:Fe columnar films to ethanol. The high performances are explained based on excellent catalytic properties of mixed phases AgO/Ag NPs, which accelerate the oxidizing reactions of ethanol molecules on the surface of nanostructured films. These results are of significant importance to the development of nanomaterials for the sensing of volatile organic compounds, e.g. ethanol vapor in modern cars with 'alcolocks', etc..

In this study we also have reported the construction of the pristine and modified ZnO $(10\bar{1}0)$ surface followed by the adsorption of small molecules. We have modelled the two stoichiometric, symmetric and non-polar terminations of the ZnO $(10\bar{1}0)$ surface. The two surface terminations were doped with Fe in the exposed 2- and 4-fold Zn lattice sites. The thermodynamically most stable surface termination, with the Fe dopant in the 2-coordinated position, was decorated with $(AgO)_m$ clusters of different sizes and at various positions. The clustering energy shows that for $m \geq 4$ the $(AgO)_m$ particles prefer to grow rather than wet the surface.

We also have investigated the interaction of H_2, CH_4, CH_3CHO and CH_3CH_2OH with the $(AgO)_5$ cluster, surface and their interface. In general, the non-polar H_2 and CH_4 molecules interact weakly with any fragment of the fully modified surface. Although CH_3CHO binds relatively strongly to the surface, we found that the nanoparticles do not enhance its adsorption as they do not provide the most stable adsorption site. Yet, the nanoparticles are fundamental for the molecular adsorption and dehydrogenation of CH_3CH_2OH, improving the sensing capabilities compared to the undecorated surface.

Acknowledgements

Dr. Lupan acknowledges the Alexander von Humboldt Foundation for the research fellowship for experienced researchers 3-3MOL/1148833 STP at the Institute for Materials Science, Kiel University, Germany. This research was sponsored partially by the German Research Foundation (DFG) under the schemes FOR2093, SFB1261, A5, A6; KI1263/12-2 and by Project SFB859. This research was partly supported by the STCU within the Grant 6229. We acknowledge the Engineering and Physical Sciences Research Council (EPSRC grant EP/K009567) for funding. Via our membership of the UK's HEC Materials Chemistry Consortium, which is funded by EPSRC (EP/L000202), this work used the ARCHER UK National Supercomputing Service (http://www.archer.ac.uk). This work was performed using the computational facilities of the Advanced Research Computing @ Cardiff (ARCCA) Division, Cardiff University. The authors also acknowledge the use of HPC Wales, Supercomputing Wales and associated support services in the completion of this work. All data created during this research is openly available from the Cardiff University's Research Portal at http://doi.org/10.17035/d.2018.0054411689

Author Contributions

V.P., A.V. and O.L. synthesized the Ag-functionalized ZnO:Fe nanomaterial. O.L. developed synthesis from chemical solution procedure SCS for ZnO. O.L., V.P., A.V. and F.S. adapted technological approach for material synthesis and integration/fabrication of the sensors. A.V., O.P., T.S. and F.F. developed functionalization procedure, set-up and realized all experiments and XPS analysis. P.V. and O.L. carried out the measurement of sensing properties of sensors based on such structures and analyzed data. J.S. and L.K. studied TEM. V.P., O.L., F.S., R.A., M.B. and P.V. analyzed the results, including Raman data and revised draft. N.H.L., D.S.C. and A.C.E. realized computational part. P.V., A.V., D.S.C., O.P and O.L. drafting the article. O.L., F.F., N.H.L., L.K. and R.A. study conception and design, final approval of the version to be published. All authors reviewed the manuscript.

References

1. L. Ma, S. Y. Ma, H. Kang, X. F. Shen, T. T. Wang, X. H. Jiang and Q. Chen, Preparation of Ag-doped ZnO-SnO_2 hollow nanofibers with an enhanced ethanol sensing performance by electrospinning, *Mater. Lett.*, 2017, **209**, 188-192.
2. H. Palneedi, H. Park Jung, D. Maurya, M. Peddigari, G. T. Hwang, V. Annapureddy, J. W. Kim, J. J. Choi, B. D. Hahn, S. Priya, J. Lee Keon and J. Ryu, Laser Irradiation of Metal Oxide Films and Nanostructures: Applications and Advances, *Adv. Mater.*, 2018, **30**, 1705148.
3. S. Park Sung and C. S. Ha, Hollow Mesoporous Functional Hybrid Materials: Fascinating Platforms for Advanced Applications, *Adv. Funct. Mater.*, 2017, **0**, 1703814.
4. T. Tung Tran, J. Nine Md, M. Krebsz, T. Pasinszki, J. Coghlan Campbell, N. H. Tran Diana and D. Losic, Recent Advances in Sensing Applications of Graphene Assemblies and Their Composites, *Adv. Funct. Mater.*, 2017, **27**, 1702891.
5. V. Dua, S. P. Surwade, S. Ammu, S. R. Agnihotra, S. Jain, K. E. Roberts, S. Park, R. S. Ruoff and S. K. Manohar, All-organic vapor sensor using inkjet-printed reduced graphene oxide, *Angew. Chem., Int. Ed.*, 2010, **49**, 2154-2157.
6. J. Guo, J. Zhang, M. Zhu, D. Ju, H. Xu and B. Cao, High-performance gas sensor based on ZnO nanowires functionalized by Au nanoparticles, *Sens. Actuators, B*, 2014, **199**, 339-345.
7. M. Naderi Nasrabadi, Y. Mortazavi and A. A. Khodadadi, Highly sensitive and selective Gd_2O_3-doped SnO_2 ethanol sensors synthesized by a high temperature and pressure solvothermal method in a microreactor, *Sens. Actuators, B*, 2016, **230**, 130-139.
8. A. Mirzaei, K. Janghorban, B. Hashemi, M. Bonyani, S. G. Leonardi and G. Neri, Highly stable and selective ethanol sensor based on α-Fe_2O_3 nanoparticles prepared by Pechini sol–gel method, *Ceram. Int.*, 2016, **42**, 6136-6144.
9. Y. Wei, X. Wang, G. Yi, L. Zhou, J. Cao, G. Sun, Z. Chen, H. Bala and Z. Zhang, Hydrothermal synthesis of Ag modified ZnO nanorods and their enhanced ethanol-sensing properties, *Mater. Sci. Semicond. Process.*, 2018, **75**, 327-333.
10. Z. Zhu, C.-T. Kao and R.-J. Wu, A highly sensitive ethanol sensor based on Ag@TiO_2 nanoparticles at room temperature, *Appl. Surf. Sci.*, 2014, **320**, 348-355.
11. V. Postica, J. Gröttrup, R. Adelung, O. Lupan, A. K. Mishra, N. H. de Leeuw, N. Ababii, J. F. C. Carreira, J. Rodrigues, N. B. Sedrine, M. R. Correia, T. Monteiro, V. Sontea and Y. K. Mishra, Multifunctional materials: A case study of the effects of metal doping on ZnO tetrapods with bismuth and tin oxides, *Adv. Funct. Mater.*, 2017, **27**, 1604676.
12. O. Lupan, V. Postica, F. Labat, I. Ciofini, T. Pauporté and R. Adelung, Ultra-sensitive and selective hydrogen nanosensor with fast response at room temperature based on a single Pd/ZnO nanowire, *Sens. Actuators, B*, 2018, **254**, 1259-1270.
13. V. Postica, F. Schütt, R. Adelung and O. Lupan, Schottky diode based on a single carbon–nanotube–ZnO hybrid tetrapod for selective sensing applications, *Adv. Mater. Int.*, 2017, **4**, 1700507.
14. V. Postica, I. Hölken, V. Schneider, V. Kaidas, O. Polonskyi, V. Cretu, I. Tiginyanu, F. Faupel, R. Adelung and O. Lupan, Multifunctional device based on ZnO:Fe nanostructured

films with enhanced UV and ultra-fast ethanol vapour sensing, *Mater. Sci. Semicond. Process.*, 2016, **49**, 20-33.
15. M. Gholami, A. A. Khodadadi, A. Anaraki Firooz and Y. Mortazavi, In_2O_3–ZnO nanocomposites: High sensor response and selectivity to ethanol, *Sens. Actuators, B*, 2015, **212**, 395-403.
16. I. Paulowicz, V. Postica, O. Lupan, N. Wolff, S. Shree, A. Cojocaru, M. Deng, Y. K. Mishra, I. Tiginyanu, L. Kienle and R. Adelung, Zinc oxide nanotetrapods with four different arm morphologies for versatile nanosensors, *Sens. Actuators, B*, 2018, **262**, 425-435.
17. J. Ding, J. Zhu, P. Yao, J. Li, H. Bi and X. Wang, Synthesis of ZnO–Ag hybrids and their gas-sensing performance toward ethanol, *Ind. Eng. Chem. Res.*, 2015, **54**, 8947-8953.
18. V. K. Tomer and S. Duhan, Ordered mesoporous Ag-doped TiO_2/SnO_2 nanocomposite based highly sensitive and selective VOC sensors, *J. Mater. Chem. A*, 2016, **4**, 1033-1043.
19. O. Lupan, F. Schütt, V. Postica, D. Smazna, Y. K. Mishra and R. Adelung, Sensing performances of pure and hybridized carbon nanotubes-ZnO nanowire networks: A detailed study, *Sci. Rep.*, 2017, **7**, 14715.
20. F. Schütt, V. Postica, R. Adelung and O. Lupan, Single and networked ZnO–CNT hybrid tetrapods for selective room-temperature high-performance ammonia sensors, *ACS Appl. Mater. Interfaces*, 2017, **9**, 23107-23118.
21. K.-W. Kim, P.-S. Cho, S.-J. Kim, J.-H. Lee, C.-Y. Kang, J.-S. Kim and S.-J. Yoon, The selective detection of C_2H_5OH using SnO_2–ZnO thin film gas sensors prepared by combinatorial solution deposition, *Sens. Actuators, B*, 2007, **123**, 318-324.
22. T. Jinkawa, G. Sakai, J. Tamaki, N. Miura and N. Yamazoe, Relationship between ethanol gas sensitivity and surface catalytic property of tin oxide sensors modified with acidic or basic oxides, *J. Mol. Catal. A: Chem.*, 2000, **155**, 193-200.
23. J. Qu, Y. Ge, B. Zu, Y. Li and X. Dou, Transition-metal-doped p-type ZnO nanoparticle-based sensory array for instant discrimination of explosive vapors, *Small*, 2016, **12**, 1369-1377.
24. Y. Cai, H. Fan, M. Xu, Q. Li and C. Long, Fast economical synthesis of Fe-doped ZnO hierarchical nanostructures and their high gas-sensing performance, *CrystEngComm*, 2013, **15**, 7339-7345.
25. J. Gröttrup, V. Postica, N. Ababii, O. Lupan, C. Zamponi, D. Meyners, Y. K. Mishra, V. Sontea, I. Tiginyanu and R. Adelung, Size-dependent UV and gas sensing response of individual Fe_2O_3-ZnO:Fe micro- and nanowire based devices, *J. Alloys Compd.*, 2017, **701**, 920-925.
26. O. Lupan, V. Postica, J. Gröttrup, A. K. Mishra, N. H. de Leeuw and R. Adelung, Enhanced UV and ethanol vapour sensing of a single 3-D ZnO tetrapod alloyed with Fe_2O_3 nanoparticles, *Sens. Actuators, B*, 2017, **245**, 448-461.
27. A. Yu, J. Qian, H. Pan, Y. Cui, M. Xu, L. Tu, Q. Chai and X. Zhou, Micro-lotus constructed by Fe-doped ZnO hierarchically porous nanosheets: Preparation, characterization and gas sensing property, *Sens. Actuators, B*, 2011, **158**, 9-16.
28. N. L. Tarwal, A. V. Rajgure, J. Y. Patil, M. S. Khandekar, S. S. Suryavanshi, P. S. Patil, M. G. Gang, J. H. Kim and J. H. Jang, A selective ethanol gas sensor based on spray-derived Ag–ZnO thin films, *J. Mater. Sci.*, 2013, **48**, 7274-7282.
29. J. Chen, X. Yan, W. Liu and Q. Xue, The ethanol sensing property of magnetron sputtered ZnO thin films modified by Ag ion implantation, *Sens. Actuators, B*, 2011, **160**, 1499-1503.
30. Z. Wen, J. Chen, M.-H. Yeh, H. Guo, Z. Li, X. Fan, T. Zhang, L. Zhu and Z. L. Wang, Blow-driven triboelectric nanogenerator as an active alcohol breath analyzer, *Nano Energy*, 2015, **16**, 38-46.
31. Q. Xiang, G. Meng, Y. Zhang, J. Xu, P. Xu, Q. Pan and W. Yu, Ag nanoparticle embedded-ZnO nanorods synthesized via a photochemical method and its gas-sensing properties, *Sens. Actuators, B*, 2010, **143**, 635-640.
32. K. Tao, X. Han, Q. Yin, D. Wang, L. Han and L. Chen, Metal-organic frameworks-derived porous In_2O_3 hollow nanorod for high-performance ethanol gas sensor, *ChemistrySelect*, 2017, **2**, 10918-10925.
33. O. Lupan, S. Shishiyanu, L. Chow and T. Shishiyanu, Nanostructured zinc oxide gas sensors by successive ionic layer adsorption and reaction method and rapid photothermal processing, *Thin Solid Films*, 2008, **516**, 3338-3345.
34. O. Lupan, L. Chow, S. Shishiyanu, E. Monaico, T. Shishiyanu, V. Şontea, B. Roldan Cuenya, A. Naitabdi, S. Park and A. Schulte, Nanostructured zinc oxide films synthesized by successive chemical solution deposition for gas sensor applications, *Mater. Res. Bull.*, 2009, **44**, 63-69.
35. O. Lupan, S. Shishiyanu, V. Ursaki, H. Khallaf, L. Chow, T. Shishiyanu, V. Sontea, E. Monaico and S. Railean, Synthesis of nanostructured Al-doped zinc oxide films on Si for solar cells applications, *Sol. Energy Mater. Sol. Cells*, 2009, **93**, 1417-1422.
36. H. Haberland, M. Karrais, M. Mall and Y. Thurner, Thin films from energetic cluster impact: A feasibility study, *J. Vac. Sci. Technol. A Vacuum, Surfaces, Film*, 1992, **10**, 3266-3271.
37. P. Solař, O. Polonskyi, A. Olbricht, A. Hinz, A. Shelemin, O. Kylián, A. Choukourov, F. Faupel and H. Biederman, Single-step generation of metal-plasma polymer multicore@shell nanoparticles from the gas phase, *Sci. Rep.*, 2017, **7**, 8514.
38. A. Vahl, J. Strobel, W. Reichstein, O. Polonskyi, T. Strunskus, L. Kienle and F. Faupel, Single target sputter deposition of alloy nanoparticles with adjustable composition via a gas aggregation cluster source, *Nanotechnol.*, 2017, **28**, 175703.
39. O. Polonskyi, T. Peter, A. Mohammad Ahadi, A. Hinz, T. Strunskus, V. Zaporojtchenko, H. Biederman and F. Faupel, Huge increase in gas phase nanoparticle generation by pulsed direct current sputtering in a reactive gas admixture, *Appl. Phys. Lett.*, 2013, **103**, 033118.
40. Y. Huttel, *Gas-phase synthesis of nanoparticles*, John Wiley & Sons, 2017.
41. I. Singh, S. Dey, S. Santra, K. Landfester, R. Muñoz-Espí and A. Chandra, Cerium-Doped Copper(II) Oxide Hollow Nanostructures as Efficient and Tunable Sensors for Volatile Organic Compounds, *ACS Omega*, 2018, **3**, 5029-5037.
42. M. Hoppe, N. Ababii, V. Postica, O. Lupan, O. Polonskyi, F. Schütt, S. Kaps, L. F. Sukhodub, V. Sontea, T. Strunskus, F. Faupel and R. Adelung, (CuO-Cu_2O)/ZnO:Al heterojunctions for volatile organic compound detection, *Sens. Actuators, B*, 2018, **255**, 1362-1375.

43. T. Peter, S. Rehders, U. Schürmann, T. Strunskus, V. Zaporojtchenko and F. Faupel, High rate deposition system for metal-cluster/$SiO_xC_yH_z$ –polymer nanocomposite thin films, *J. Nanopart. Res.*, 2013, **15**, 1710.
44. V. Cretu, V. Postica, A. K. Mishra, M. Hoppe, I. Tiginyanu, Y. K. Mishra, L. Chow, N. H. de Leeuw, R. Adelung and O. Lupan, Synthesis, characterization and DFT studies of zinc-doped copper oxide nanocrystals for gas sensing applications, *J. Mater. Chem. A*, 2016, **4**, 6527-6539.
45. O. Lupan, V. Cretu, V. Postica, N. Ababii, O. Polonskyi, V. Kaidas, F. Schütt, Y. K. Mishra, E. Monaico, I. Tiginyanu, V. Sontea, T. Strunskus, F. Faupel and R. Adelung, Enhanced ethanol vapour sensing performances of copper oxide nanocrystals with mixed phases, *Sens. Actuators, B*, 2016, **224**, 434-448.
46. R. Cuscó, E. Alarcón-Lladó, J. Ibáñez, L. Artús, J. Jiménez, B. Wang and M. J. Callahan, Temperature dependence of Raman scattering in ZnO, *Phys. Rev. B*, 2007, **75**, 165202.
47. G. I. N. Waterhouse, G. A. Bowmaker and J. B. Metson, The thermal decomposition of silver (I, III) oxide: A combined XRD, FT-IR and Raman spectroscopic study, *Phys. Chem. Chem. Phys.*, 2001, **3**, 3838-3845.
48. O. Lupan, V. Postica, R. Adelung, F. Labat, I. Ciofini, U. Schürmann, L. Kienle, L. Chow, B. Viana and T. Pauporté, Functionalized Pd/ZnO nanowires for nanosensors, *Phys. Status Solidi RRL*, 2018, **12**, 1700321.
49. G. Greczynski and L. Hultman, C 1s Peak of Adventitious Carbon Aligns to the Vacuum Level: Dire Consequences for Material's Bonding Assignment by Photoelectron Spectroscopy, *ChemPhysChem*, 2017, **18**, 1507-1512.
50. V. Postica, M. Hoppe, J. Gröttrup, P. Hayes, V. Röbisch, D. Smazna, R. Adelung, B. Viana, P. Aschehoug, T. Pauporté and O. Lupan, Morphology dependent UV photoresponse of Sn-doped ZnO microstructures, *Solid State Sci.*, 2017, **71**, 75-86.
51. NIST X-ray photoelectron spectroscopy database, NIST standard reference database number 20, *National Institute of Standards and Technology, Gaithersburg MD*, 2000, **20899**, doi:10.18434/T18434T18488K.
52. H. Hofmeister, Fivefold twinned nanoparticles, *Encyclopedia of Nanoscience and Nanotechnology* 2004, **3**, 431-452.
53. J. P. Franey, G. W. Kammlott and T. E. Graedel, The corrosion of silver by atmospheric sulfurous gases, *Corros. Sci.*, 1985, **25**, 133-143.
54. N. Rossler, K. Kotsis and V. Staemmler, Ab initio calculations for the Zn 2s and 2p core level binding energies in Zn oxo compounds and ZnO, *Phys. Chem. Chem. Phys.*, 2006, **8**, 697-706.
55. A. J. Varkey and A. F. Fort, Some optical properties of silver peroxide (AgO) and silver oxide (Ag_2O) films produced by chemical-bath deposition, *Sol. Energy Mater. Sol. Cells*, 1993, **29**, 253-259.
56. Z. Zhao and M. A. Carpenter, Support-free bimodal distribution of plasmonically active Ag/AgO_x nanoparticle catalysts: Attributes and plasmon enhanced surface chemistry, *J. Phys. Chem. C*, 2013, **117**, 11124-11132.
57. L. A. Currie, Nomenclature in evaluation of analytical methods including detection and quantification capabilities (IUPAC Recommendations 1995), *Pure App. Chem.*, 1995, **67**, 1699-1723.
58. N. Bârsan and U. Weimar, Understanding the fundamental principles of metal oxide based gas sensors; the example of CO sensing with SnO_2 sensors in the presence of humidity, *J. Phys. Cond. Matter*, 2003, **15**, R813.
59. O. Lupan, L. Chow, T. Pauporté, L. K. Ono, B. Roldan Cuenya and G. Chai, Highly sensitive and selective hydrogen single-nanowire nanosensor, *Sens. Actuators, B*, 2012, **173**, 772-780.
60. N. Barsan and U. Weimar, Conduction model of metal oxide gas sensors, *J. Electroceram.*, 2001, **7**, 143-167.
61. J. Gröttrup, V. Postica, D. Smazna, M. Hoppe, V. Kaidas, Y. K. Mishra, O. Lupan and R. Adelung, UV detection properties of hybrid ZnO tetrapod 3-D networks, *Vacuum*, 2017, **146**, 492-500.
62. O. Lupan, V. Postica, J. Gröttrup, A. K. Mishra, N. H. de Leeuw, J. F. C. Carreira, J. Rodrigues, N. Ben Sedrine, M. R. Correia, T. Monteiro, V. Cretu, I. Tiginyanu, D. Smazna, Y. K. Mishra and R. Adelung, Hybridization of zinc oxide tetrapods for selective gas sensing applications, *ACS Appl. Mater. Interfaces*, 2017, **9**, 4084-4099.
63. X. Chen, Z. Guo, W.-H. Xu, H.-B. Yao, M.-Q. Li, J.-H. Liu, X.-J. Huang and S.-H. Yu, Templating synthesis of SnO_2 nanotubes loaded with Ag_2O nanoparticles and their enhanced gas sensing properties, *Adv. Funct. Mater.*, 2011, **21**, 2049-2056.
64. E. H. Kisi and M. M. Elcombe, *u* parameters for the wurtzite structure of ZnS and ZnO using powder neutron diffraction, *Acta Crystallogr. Sect. C Cryst. Struct. Commun.*, 1989, **45**, 1867-1870.
65. R. Bader, *Journal*, 1990.
66. G. Henkelman, A. Arnaldsson and H. Jónsson, A fast and robust algorithm for Bader decomposition of charge density, *Comput. Mater. Sci.* , 2006, **36**, 354-360.
67. E. Sanville, D. Kenny Steven, R. Smith and G. Henkelman, Improved grid-based algorithm for Bader charge allocation, *J. Comput. Chem.*, 2007, **28**, 899-908.
68. W. Tang, E. Sanville and G. Henkelman, A grid-based Bader analysis algorithm without lattice bias, *J. Phys. Condens. Matter* 2009, **21**, 084204.
69. D. Santos-Carballal, A. Roldan, R. Grau-Crespo and N. H. de Leeuw, First-principles study of the inversion thermodynamics and electronic structure of FeM_2X_4 (thio)spinels (M = Cr, Mn, Co, Ni; X = O, S), *Phys. Rev. B*, 2015, **91**, 195106.
70. D. Santos-Carballal, P. E. Ngoepe and N. H. de Leeuw, Ab initio investigation of the thermodynamics of cation distribution and of the electronic and magnetic structures in the $LiMn_2O_4$ spinel, *Phys. Rev. B*, 2018, **97**, 085126.
71. R. Escudero and R. Escamilla, Ferromagnetic behavior of high-purity ZnO nanoparticles, *Solid State Commun.*, 2011, **151**, 97-101.
72. T. Han, F. Y. Meng, S. Zhang, X. M. Cheng and J. I. Oh, Band gap and electronic properties of wurtzite-structure ZnO co-doped with IIA and IIIA, *J. Appl. Phys.*, 2011, **110**, 063724.
73. V. Scatturin, P. L. Bellon and A. J. Salkind, The structure of silver oxide determined by means of neutron diffraction, *J. Electrochem. Soc.*, 1961, **108**, 819-822.

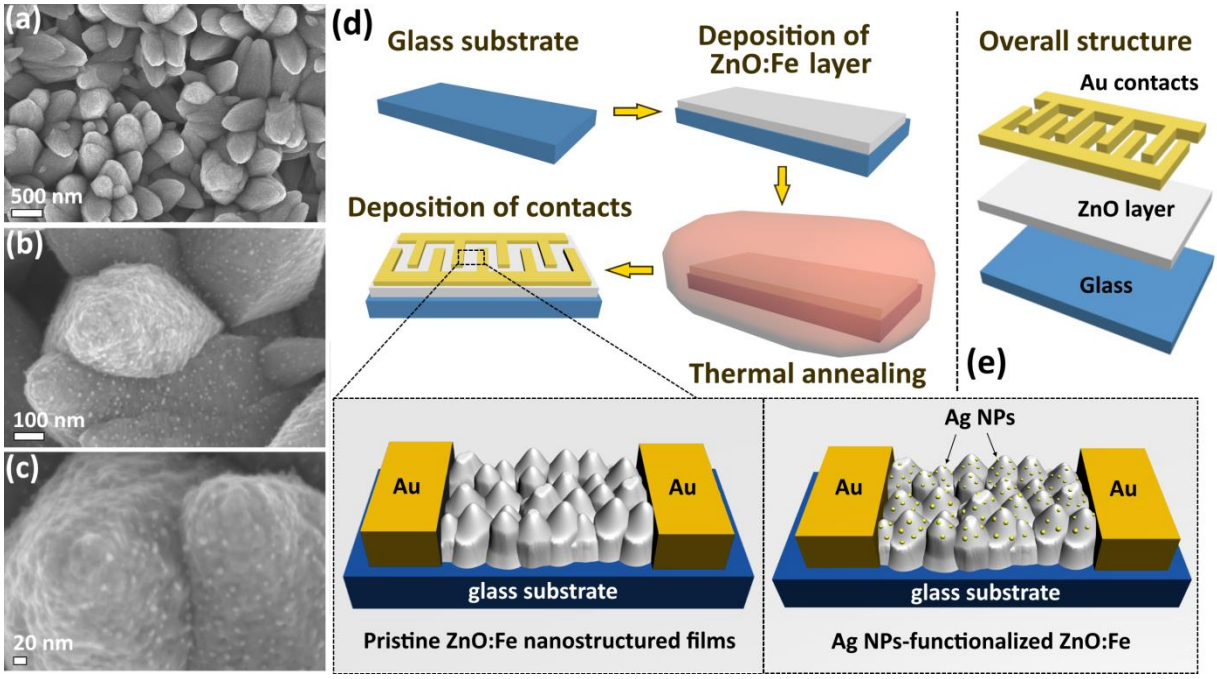

Figure 1. SEM images of - nanostructured ZnO:Fe columnar films decorated with AgO/Ag nanoparticles: (a) at low magnification; (b,c) at higher magnification. (d) Illustration of fabrication flow of gas sensors based on ZnO:Fe and AgO/Ag NPs-functionalized ZnO:Fe columnar films and (e) the overall structure of sensor.

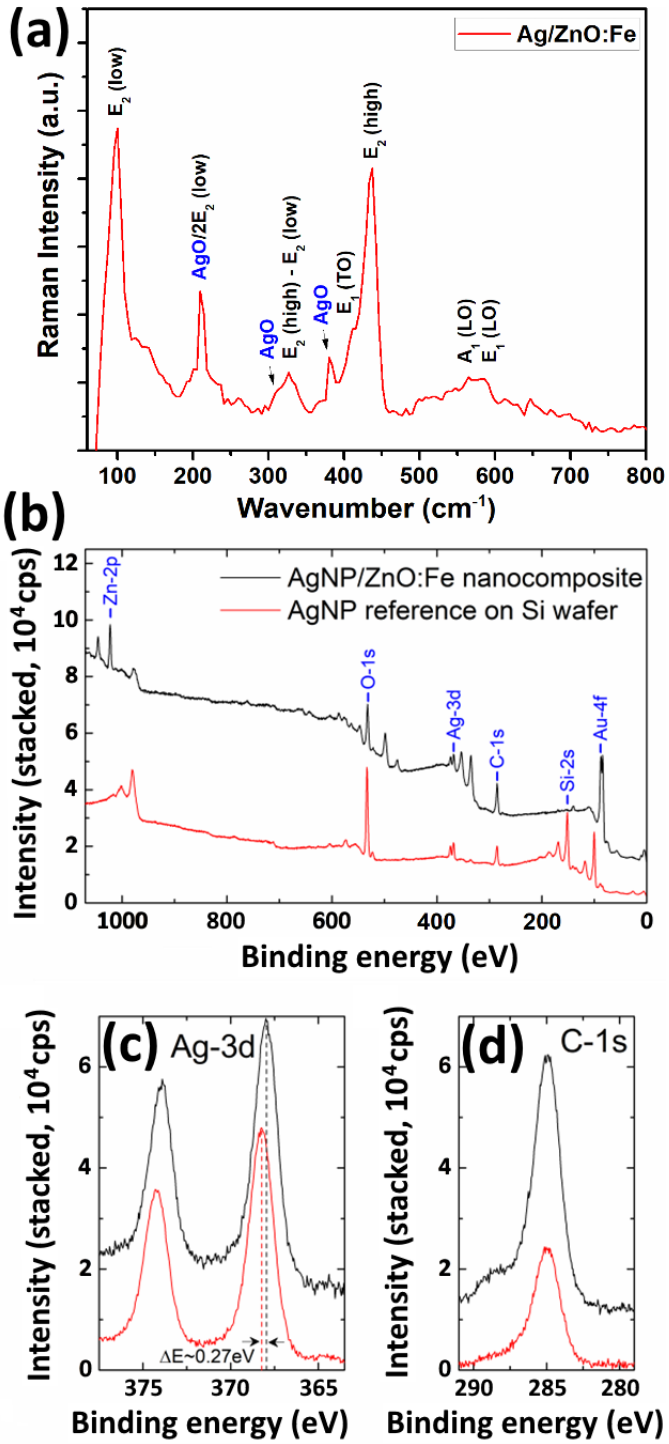

Figure 2. (a) Room temperature micro-Raman spectrum of AgO/Ag-functionalized ZnO:Fe columnar film. XPS spectra of AgO/Ag/ZnO:Fe nanocomposite (black, upper line) and reference AgNP (red, lower line); (b) overview spectra; (c) high resolution spectra of Ag-3d lines; (d) high resolution spectra of C-1s line.

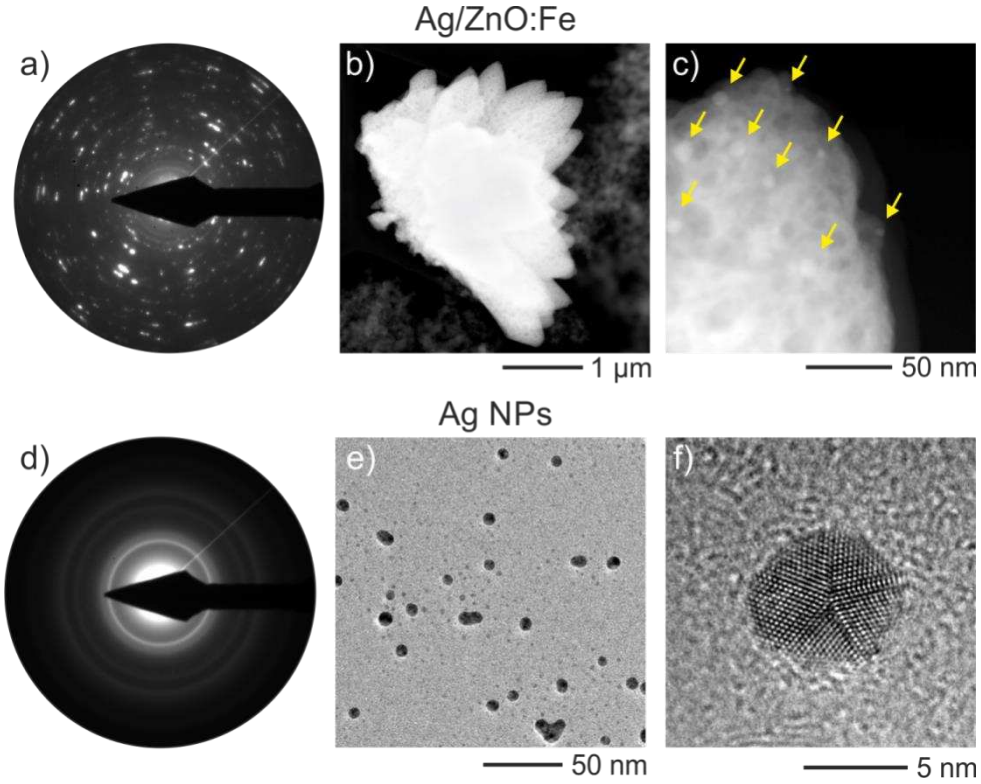

Figure 3. TEM analysis of Ag/ZnO:Fe (top row) and Ag NPs on carbon films as a reference (bottom row). a) SAED pattern of Ag/ZnO:Fe crystals. The *d*-values determined from the pattern match with wurtzite-structure ZnO, pure Ag and AgO (space group $P2_1/c$). b) and c) STEM-HAADF images of a ZnO:Fe crystal cluster. Yellow arrows in c) mark position of Ag NPs. d) SAED pattern of Ag NPs on a blank carbon film. Only *d*-values associated with pure Ag are apparent. e) TEM bright field image of the clusters, showing the pronounced bimodal size distribution. f) High resolution micrograph of a silver nanoparticle.

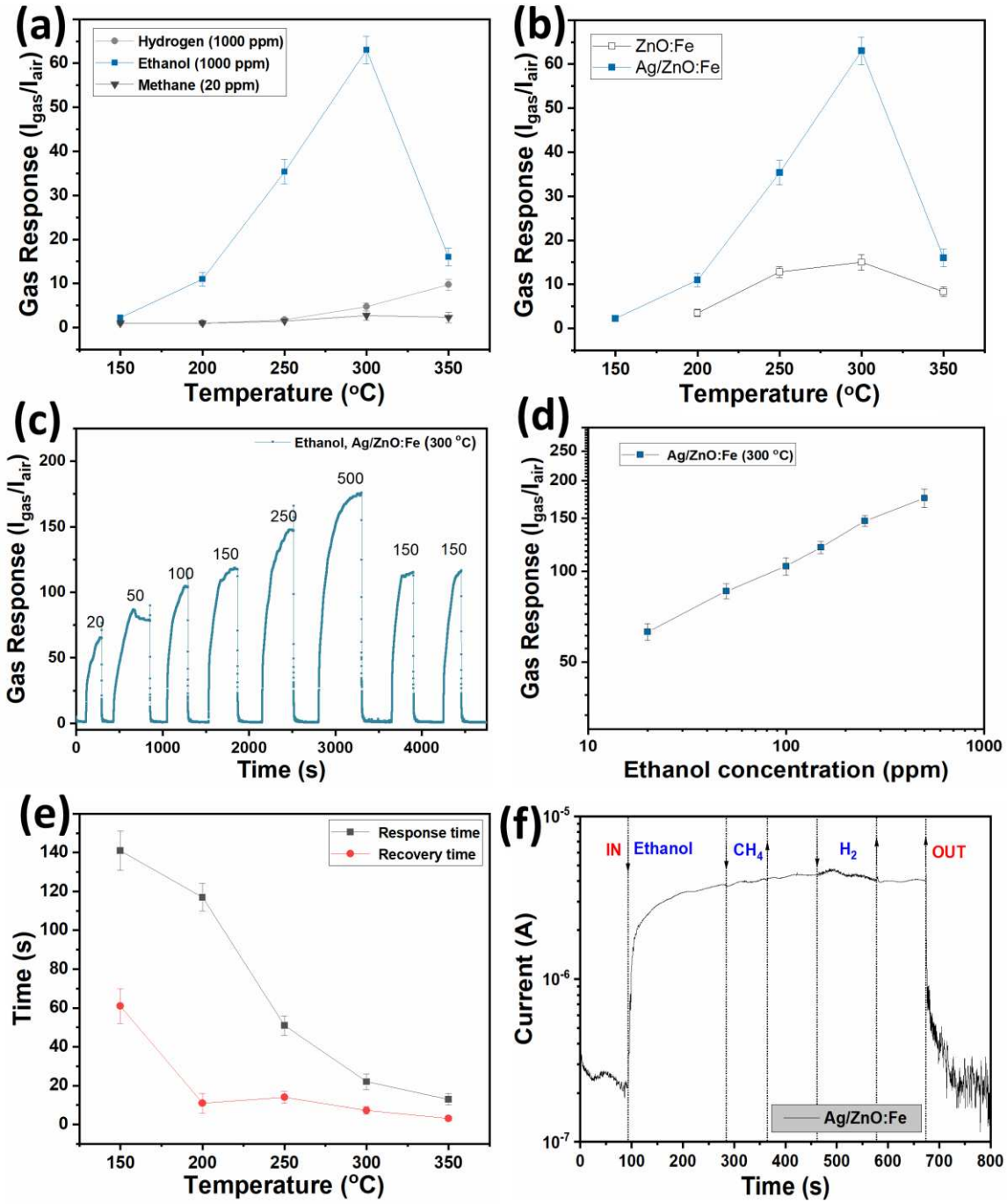

Figure 4. (a) Gas response versus operating temperature of columnar Ag/ZnO:Fe film. (b) Gas response to 20 ppm of ethanol vapors versus operating temperature of ZnO:Fe and Ag/ZnO:Fe columnar film. (c) Dynamic response of Ag/ZnO:Fe structure to different concentrations of ethanol vapors at 300 ºC of operating temperature. (d) Gas response of Ag/ZnO:Fe films versus concentration of ethanol vapors at 300 ºC of operating temperature. (e) Calculated response and recovery times of Ag/ZnO:Fe structure versus operating temperature. (f) Dynamic response to 1000 ppm of CH_4 and H_2 in the air + ethanol vapors with 20 ppm of AgO/Ag/ZnO:Fe structure.

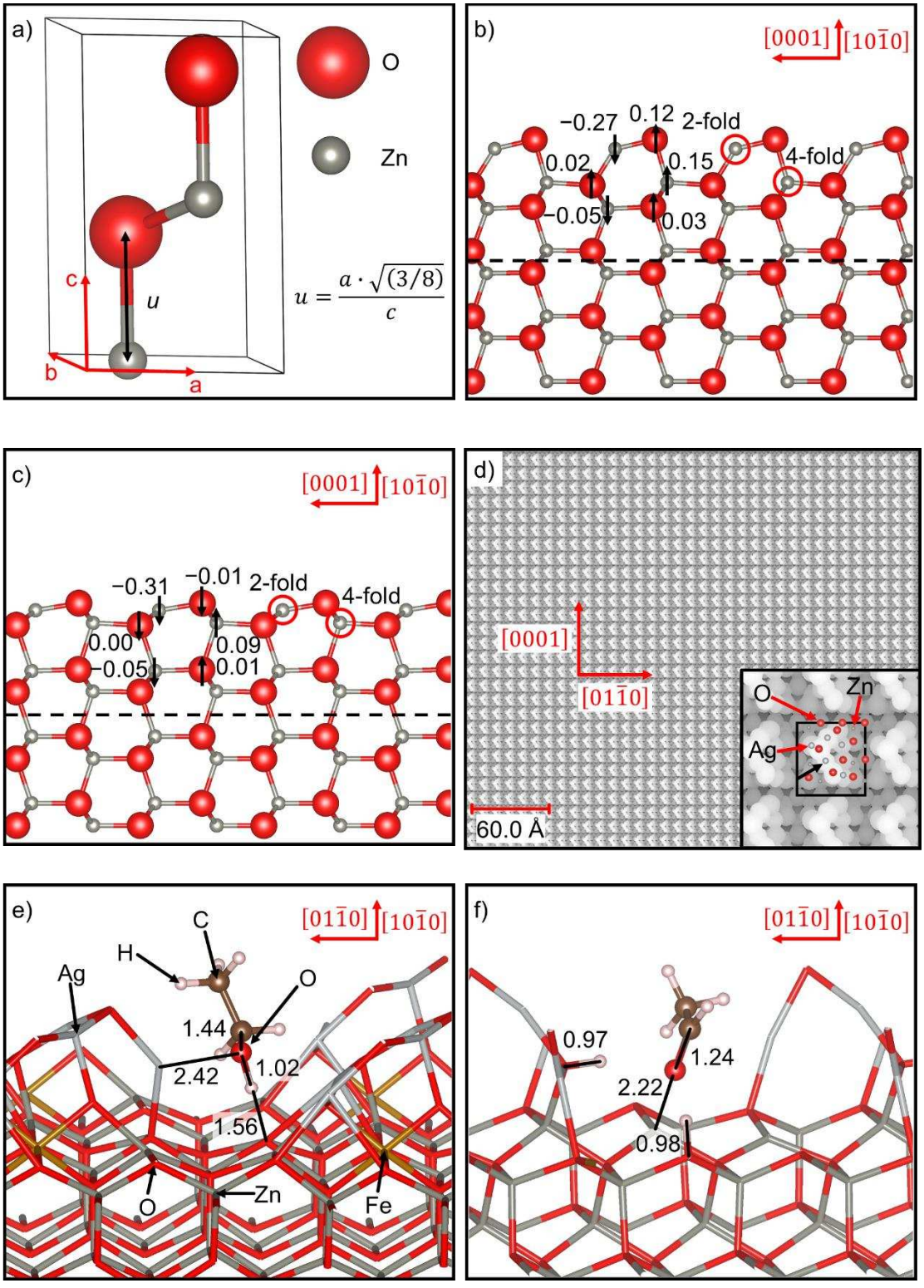

Figure 5. Schematic representation of: (a) the conventional hexagonal unit cell containing two formula units of wurtzite ZnO, where the mathematical relationship for the oxygen *u* parameter is indicated. Side

view of the relaxed simulation slabs of terminations: (b) A and (c) B of the ZnO $(10\bar{1}0)$ surface. Black arrows show the direction in which the surface atoms moved during optimisation and the numbers indicate the displacement in Å in the direction perpendicular to the surface. Negative values represent movement towards the bulk, while positive numbers denote displacement towards the vacuum. The 2- and 4-fold Zn positions that were doped with Fe are displayed within red circles, and the dashed line represents the plane of symmetry. (d) Simulated STM image of the Fe-doped ZnO $(10\bar{1}0)$ surface with the $(AgO)_5$ cluster adsorbed using a bias of −2.0 eV, a density of 0.0186 e·Å^{-3} and a tip distance of 1.50 Å. Inset shows enlargement of the STM image. The black arrow indicates the position of the Fe dopant below the $(AgO)_5$ nanoparticle. (e) Molecular adsorption of ethanol and (f) dehydrogenated adsorption of ethanol. Interatomic distances are represented in Å. Crystallographic directions are indicated for all figures.